This is a preprint, the final version is subject to change, of the American Mineralogist (MSA)
Cite as Authors (Year) Title. American Mineralogist, in press.
DOI: https://doi.org/10.2138/am-2018-6267

REVISION 1

Equations of state and phase boundary for stishovite and $CaCl_2$-type SiO_2

Rebecca A. Fischer[1,2,3,4,*], Andrew J. Campbell[1], Bethany A. Chidester[1,5], Daniel M. Reaman[1], Elizabeth C. Thompson[1], Jeffrey S. Pigott[6,7], Vitali B. Prakapenka[8], and Jesse S. Smith[9]

[1]University of Chicago, Department of the Geophysical Sciences, 5734 S Ellis Ave, Chicago, IL 60637, USA

[2]Smithsonian Institution, National Museum of Natural History, Department of Mineral Sciences, PO Box 37012, MRC 119, Washington, DC 20013-7012, USA

[3]University of California Santa Cruz, Department of Earth and Planetary Sciences, 1156 High St, Santa Cruz, CA 95064, USA

[4]Harvard University, Department of Earth and Planetary Sciences, 20 Oxford St, Cambridge, MA 02138, USA

[5]Now at: University of California Davis, Department of Earth and Planetary Sciences, 1 Shields Ave, Davis, CA 95616, USA

[6]Ohio State University, School of Earth Sciences, 125 S Oval Mall, Columbus, OH 43210, USA

[7]Now at: Case Western Reserve University, Department of Earth, Environmental, and Planetary Sciences, 10900 Euclid Ave, Cleveland, OH 44106

[8]University of Chicago, Center for Advanced Radiation Sources, 5640 S Ellis Ave, Chicago, IL 60637, USA

[9]High Pressure Collaborative Access Team (HPCAT), Geophysical Laboratory, Carnegie Institution of Washington, 9700 S Cass Ave, Argonne, IL 60439, USA

*Corresponding author. Email: rebeccafischer@g.harvard.edu

Submitted to *American Mineralogist*, 3 August 2017

Revised version submitted 31 December 2017

Abstract

Silica is thought to be present in the Earth's lower mantle in subducting plates, in addition to being a prototypical solid whose physical properties are of broad interest. It is known to undergo a phase transition from stishovite to the $CaCl_2$-type structure at ~50–80 GPa, but the exact location and slope of the phase boundary in pressure-temperature space is unresolved. There have been many previous studies on the equation of state of stishovite, but they span a limited range of pressures and temperatures, and there has been no thermal equation of state of $CaCl_2$-type SiO_2 measured under static conditions. We have investigated the phase diagram and equations of state of silica at 21–89 GPa and up to ~3300 K using synchrotron X-ray diffraction in a laser-heated diamond anvil cell. The phase boundary between stishovite and $CaCl_2$-type SiO_2 can be approximately described as $T = 64.6(49)*P - 2830(350)$, with temperature T in Kelvin and pressure P in GPa. The stishovite data imply $K_0' = 5.24(9)$ and a quasi-anharmonic T^2 dependence of $-6.0(4) \times 10^{-6}$ GPa*cm^3/mol/K^2 for a fixed $q = 1$, $\gamma_0 = 1.71$, and $K_0 = 302$ GPa, while for the $CaCl_2$-type phase $K_0 = 341(4)$ GPa, $K_0' = 3.20(16)$, and $\gamma_0 = 2.14(4)$ with other parameters equal to their values for stishovite. The behaviors of the *a* and *c* axes of stishovite with pressure and temperature were also fit, indicating a much more compressible *c* axis with a lower thermal expansion as compared to the *a* axis. The phase transition between stishovite and

47 $CaCl_2$-type silica should occur at pressures of 68–78 GPa in the Earth, depending on the
48 temperature in subducting slabs. Silica is denser than surrounding mantle material up to
49 pressures of 58–68 GPa, with uncertainty due to temperature effects; at higher pressures than
50 this, SiO_2 becomes gravitationally buoyant in the lower mantle.
51
52 **Keywords:** silica, SiO_2, stishovite, phase diagram, equation of state, phase transition, X-ray
53 diffraction
54

55 1. Introduction

56 Silica (SiO_2) is expected to be present in subducted mid-ocean ridge basalt in the Earth's
57 lower mantle (e.g., Hirose et al. 2005). It may also occur in the D″ layer as a result of Si and O
58 becoming less soluble in liquid iron as the core cools (Hirose et al. 2017), since the metal–
59 silicate partitioning of O and especially Si are strongly temperature dependent (e.g., Fischer et al.
60 2015; Tsuno et al. 2013). Despite its importance in geophysics, as well as physics and materials
61 science, there remains disagreement surrounding the phase diagram of silica at high pressures (P)
62 and temperatures (T). Additionally, only limited research has been done on the thermal equation
63 of state for the $CaCl_2$-type phase of silica, stable under lower mantle conditions. In this study, we
64 focus on elucidating the location and slope of the stishovite/$CaCl_2$-type phase boundary, as well
65 as providing better constraints on the thermal equations of state of these important phases.
66 Coesite (monoclinic SiO_2 with space group *C2/c*) transforms to stishovite (rutile-type
67 SiO_2 with space group $P4_2/mnm$) at ~7–13 GPa and high temperatures (e.g., Zhang et al. 1996),
68 marking a transition in Si coordination from tetrahedral to octahedral. At lower mantle pressures,
69 stishovite undergoes a second order, reversible phase transition to the $CaCl_2$-type structure

(space group *Pnnm*) of SiO_2, in which the tetragonal unit cell of stishovite distorts into an orthorhombic unit cell (Tsuchida and Yagi 1989). Reports of the location and slope of this phase boundary vary, with room temperature measurements under quasi-hydrostatic conditions on pure silica typically reporting a transition pressure of 45–55 GPa (Andrault et al. 1998; Hemley et al. 2000; Kingma et al. 1995; Nomura et al. 2010; Ono et al. 2002), in agreement with some theoretical calculations (Karki et al. 1997; Togo et al. 2008; Tsuchiya et al. 2004); the location of the phase boundary is affected by impurities such as Al and H (e.g., Lakshtanov et al. 2007). High temperature measurements indicate a positive Clapeyron slope (Akins and Ahrens 2002; Nomura et al. 2010; Ono et al. 2002) (Figure 1). The $CaCl_2$-type structure converts to seifertite (α-PbO_2-type silica) at pressures of ~120–140 GPa (Dubrovinsky et al. 1997; Grocholski et al. 2013), though there remains ambiguity over the precise location and slope of this phase boundary as well (Murakami et al. 2003; Shieh et al. 2005). The phase diagram of silica is known to be subject to kinetic barriers, especially at room temperature, with observations of a large number of metastable and/or amorphous phases. These kinetic inhibitions are dependent on the degree of hydrostaticity and the nature of the starting materials as well as temperature-pressure pathways (e.g., Asahara et al. 2013; Dubrovinsky et al. 2003; Haines et al. 2001; Hazen et al. 1989; Hemley 1987; Kingma et al. 1993; Prakapenka et al. 2004; Tsuchida and Yagi 1990).

The equation of state of stishovite has been measured numerous times since its discovery by Chao et al. (1962) (Supplemental Table S1 and references therein): at high pressures using diamond anvil cell (e.g., Andrault et al. 2003; Jiang et al. 2009; Panero et al. 2003; Pigott et al. 2015; Ross et al. 1990; Yamanaka et al. 2002), shock wave (e.g., Luo et al. 2002a; Lyzenga et al. 1983), large volume press (e.g., Liu et al. 1999; Nishihara et al. 2005; Wang et al. 2012), piston cylinder apparatus (e.g., Li et al. 1996), and computational (e.g., Cohen 1991; Driver et al. 2010;

Karki et al. 1997a; Luo et al. 2002b; Tsuchiya et al. 2004) methods, as well as on synthetic samples at ambient pressure (e.g., Brazhkin et al. 2005; Weidner et al. 1982; Yoneda et al. 2012). Despite the number of prior studies on the stishovite equation of state, it has previously only been measured to 54 GPa and 1700 K (Wang et al. 2012) or 50 GPa and 2400 K (Pigott et al. 2015), requiring extrapolation to apply these equations of state over the conditions of stishovite stability in the Earth.

The isothermal equation of state of $CaCl_2$-type SiO_2 has been previously studied in a diamond anvil cell (Andrault et al. 1998, 2003; Grocholski et al. 2013) and using computational methods (Karki et al. 1997b; Oganov et al. 2005; Yang and Wu 2014). However, the only published thermal equation of state of $CaCl_2$-type SiO_2 is based on a meta-analysis of shock wave literature data (Akins and Ahrens 2002). Some previous studies have instead fit a single equation of state to data on both the stishovite and $CaCl_2$-type structures (e.g., Yamazaki et al. 2014), assuming that the two phases have the same compressibility and thermal properties.

In this study, we use synchrotron X-ray diffraction in a laser-heated diamond anvil cell to determine the crystal structure and density of SiO_2 as a function of pressure and temperature at lower mantle conditions. This information is used to map the phase boundary between stishovite and $CaCl_2$-type SiO_2. By combining these data with previous results at room temperature, we construct thermal equations of state for both stishovite and $CaCl_2$-type SiO_2 to higher pressures (~89 GPa) and temperatures (~3300 K) than in previous work and with broader *P*-*T* coverage.

2. Experimental methods

Symmetric-type diamond anvil cells were used to generate high pressures, with either 300 μm culet anvils or beveled anvils with 150 μm flats. Starting materials were powdered

natural quartz and amorphous Pt (Alfa Aesar, 99.9%) in a ratio of ~2:1 by volume in two of our samples, while the third sample contained powdered natural quartz and spherical Pt (Alfa Aesar, 99.95%) in a ratio of ~3:1 by volume. Platinum was used to absorb the heating laser during the experiment; it was chosen because it is a strong laser absorber, is inert, and has a well-characterized equation of state (e.g., Dorogokupets and Oganov 2007). The quartz was measured with a scanning electron microscope and determined to contain no detectable Al. Samples composed of silica glass instead of natural quartz (but otherwise identical) did not sufficiently crystallize at high temperatures during the experiment. In each case, starting materials were mechanically ball-milled to grind and mix the powders. The powder mixture was then pressed into a flake ~5 μm thick and loaded into a rhenium gasket (preindented to 27–33 GPa) between two layers of KBr, each ~10–15 μm thick, which served as the pressure medium and thermal insulator. KBr was used due to its extremely efficient thermal insulating properties, hydrostaticity at high temperatures, strong X-ray fluorescence that allows for precise alignment of the X-ray and laser optics on the sample, and well-characterized equation of state while used as a thermal insulator (Fischer et al. 2012). Prior to loading, the KBr was oven dried and stored in a desiccator. The entire sample assembly was oven dried at 80–85 ºC for 30–60 minutes after loading but before closing the cell to remove any residual moisture.

Angle-dispersive synchrotron X-ray diffraction (XRD) was performed during laser heating experiments at the Advanced Photon Source, Argonne National Laboratory. Experiments were performed at Sector 13-ID-D, GeoSoilEnviro Center for Advanced Radiation Sources (GSECARS) (Shen et al. 2005; Prakapenka et al. 2008), and Sector 16-ID-B, High Pressure Collaborative Access Team (HPCAT) (Meng et al. 2015). At GSECARS, the X-ray beam was ~3 μm × 4 μm with a wavelength of 0.3344 Å, and the sample-to-detector distance was

calibrated with 1 bar diffraction of LaB_6. At HPCAT, the X-ray beam was ~5 μm × 7 μm with a wavelength of 0.4066 Å, and the sample-to-detector distance was calibrated with 1 bar diffraction of CeO_2. X-ray exposure times were 5–30 seconds.

Double-sided laser heating was performed with 1064 nm fiber lasers, focused onto each side of the sample. Before each experiment, the X-ray beam was coaligned with the temperature measurement system and heating lasers using X-ray induced fluorescence of the KBr pressure medium in the sample (after heating, it was confirmed that this alignment had been maintained). At each pressure, the temperature was slowly stepped up by increasing the laser power until a target temperature was reached, then the laser power was gradually decreased to zero, with diffraction patterns collected on heating and cooling. The sample was held fixed during heating. At each spot, a localized region of the sample was heated, and the conversion from silica (which had become amorphous upon compression) to stishovite was rapid (less than one minute). The temperature was stable during our X-ray data collection due to the subsolidus conditions. Power to the two lasers was adjusted independently to minimize axial temperature gradients. At HPCAT, the lasers had Gaussian intensity profiles and produced spots with diameters of ~40 μm (FWHM) on the samples, and at GSECARS, the lasers had "flat-top" intensity profiles created with Pi-shapers and diameters of ~25 μm on the samples. The laser-heated spots were much larger than the X-ray beam to minimize the effects of radial temperature gradients, and temperatures were measured from an area on the sample a few μm across, comparable to the size of the X-ray beam.

Temperatures were determined by spectroradiometry using the graybody approximation. The reported sample temperatures are an average of upstream and downstream temperature measurements, corrected downward by 3% to account for a small axial gradient through the

sample (Campbell et al. 2007, 2009). Reported temperature uncertainties include an analytical uncertainty of 100 K (e.g., Shen et al. 2001), the difference between the upstream and downstream temperatures, and uncertainty from the thickness correction (Campbell et al. 2007, 2009). At each beamtime, temperature measurements in the diamond anvil cell were benchmarked by first analyzing a sample of iron at high pressures (Fischer et al. 2011, 2012, 2014) to verify the location of the hcp–fcc transition (Komabayashi and Fei 2010). In each case the temperature of the transition was confirmed within uncertainty, ensuring compatibility between measurements made at different beamlines.

X-ray diffraction patterns were integrated to produce 2θ plots using Fit2D (Hammersley et al. 1996) or Dioptas (Prescher and Prakapenka 2015), and peak-fitting was performed using PeakFit (Systat Software). Lattice parameters of each phase were calculated from the measured *d*-spacings. Pressures were primarily determined from the volume of B2-KBr using its thermal equation of state, which was calibrated at room temperature and while used as a pressure medium during laser heating experiments against the equations of state of numerous materials to pressures of >100 GPa (Fischer et al. 2012); at high temperatures, KBr was mainly calibrated against the Pt equation of state of Dorogokupets and Oganov (2007). The platinum absorber also served as a secondary pressure standard in these experiments using the equation of state of Dorogokupets and Oganov (2007), but in some cases was not usable. To measure the pressure, lattice parameters and their uncertainties were determined as the average and standard deviation of 8 to 13 *d*-spacings for KBr or 2 to 6 *d*-spacings for Pt. The temperature of the KBr insulator/calibrant was corrected downward from the measured temperature to account for axial thermal gradients through the insulating layer (Campbell et al. 2009), while the temperature of the Pt was assumed to equal the sample temperature. Lattice parameters of the sample were

185 determined from 5 to 17 *d*-spacings for stishovite or 7 to 20 *d*-spacings for the $CaCl_2$-type
186 structure.
187
188 **3. Results**
189 The silica samples became amorphous (Hemley et al. 1988) or highly disordered
190 (Prakapenka et al. 2004) upon compression, and then crystallized in the stishovite or $CaCl_2$-type
191 structure upon laser-heating. SiO_2 phase identification was primarily based on the splitting of the
192 stishovite 210, 211, and 301 peaks upon transformation to the $CaCl_2$-type structure. An X-ray
193 diffraction pattern collected at 74(2) GPa and 2160(120) K is shown in Figure 2a, exhibiting the
194 stishovite structure. All of the peaks can be indexed as B2-KBr, stishovite-SiO_2, fcc-Pt, or hcp-
195 Re (from the gasket). Figure 2b shows the evolution of the stishovite 301 peak during cooling at
196 ~74 GPa. At higher temperatures, a single peak is seen; between 2160(120) K and 1870(110) K,
197 the peak splits into the $CaCl_2$-type 301 and 031 peaks, and at lower temperatures a doublet is
198 seen. In the 2D diffraction images, SiO_2 peaks often appear as spots (Figure 2b) due to Ostwald
199 ripening of the sample at high temperatures. These spots (including the $CaCl_2$-type 301 and 031
200 peaks) typically appear at random azimuthal angles; alternatively, in some instances, a single
201 stishovite 301 reflection is observed to split across the phase boundary at a fixed azimuthal angle
202 (Figure 2b insets).
203 X-ray diffraction data were collected from 21–89 GPa and up to ~3300 K (Figure 3).
204 Pressures determined from the KBr insulator and Pt absorber agree within mutual 2σ
205 uncertainties in every instance, with no systematic offset between them (Supplemental Table S2).
206 The phase transition from stishovite to the $CaCl_2$-type structure was observed at pressures of
207 ~60–80 GPa and high temperatures with a positive Clapeyron slope (Figure 3). The transition

between these phases was rapid and easily reversible. The pressures, temperatures, phase identification, and lattice parameters of all phases in this work are listed in Supplemental Table S2. While the phase transition could be observed on both heating and cooling, data collected on cooling were favored for use in equation of state fitting (Section 4.2–4.3) due to their lower deviatoric stresses. The stress state in the experiments was quasi-hydrostatic due to the high temperatures at which the data were collected. This can be seen, for example, by comparing the Pt peak widths in these experiments to those measured at room temperature in He or Ne (e.g., Dorfman et al. 2012), with the latter being much broader.

4. Discussion

4.1. Phase transition in silica

The location and slope of the phase boundary between stishovite and $CaCl_2$-type SiO_2 has been constrained (Figure 3); it can be approximately described as $T = 64.6(49)*P - 2830(350)$, with temperature in Kelvin and pressure in GPa. The covariance between the two fitted parameters is –1690. The covariance between two parameters a and b can be translated into a correlation coefficient, defined as $r = \text{covariance}(a,b) / (\sigma_a * \sigma_b)$. The correlation coefficient varies between –1 (perfect negative correlation) and +1 (perfect positive correlation), with a value of zero indicating no correlation. The correlation coefficient between the slope and intercept of our phase boundary is $r = –0.99$, indicating a near-perfect anticorrelation between them. Figure 1 compares the phase boundary from this work to those reported in the literature. It lies in the same region of P-T space as those of previous studies, agreeing best with the boundary of Ono et al. (2002) at pressures of ~65–85 GPa and with the boundaries of Nomura et al. (2010) and Yamazaki et al. (2014) at pressures below ~60 GPa. These data are consistent with

observations of the $CaCl_2$-type phase from Shieh et al. (2005) at 73–75 GPa, and with most of the observations of the stishovite phase from Wang et al. (2012).

The boundary presented here has a slightly shallower slope than those of previous studies, with reported values of approximately 83 K/GPa (Ono et al. 2002), 89 K/GPa (Nomura et al. 2010), 129 K/GPa (Yamazaki et al. 2014), and 180 K/GPa (Akins and Ahrens 2002). An extrapolation of this phase boundary to 300 K yields a predicted transition pressure of 49 GPa. This value agrees with some reported transition pressures at 300 K within uncertainty (Grocholski et al. 2013; Hemley et al. 2000; Kingma et al. 1995; Nomura et al. 2010; Yamazaki et al. 2014) (Figure 1), while other experimental studies report higher transition pressures (Andrault et al. 1998; Ono et al. 2002; Wang et al. 2012), which could be due to slow kinetics at room temperature, since kinetics are known to play a role in the SiO_2 phase diagram (e.g., Prakapenka et al. 2004). Some previous high temperature studies anchored their phase boundary to a measured transition pressure at 300 K (e.g., Akins and Ahrens 2002; Ono et al. 2002). These kinetic inhibitions may result in an overestimate of the transition pressure at 300 K, which may explain the slightly shallower slope reported here. The difference in slope may also be related to the very strong anticorrelation between the slope and intercept of the phase boundary; a higher transition pressure at 300 K would produce a steeper slope. The data in this study cross the stishovite–$CaCl_2$-type SiO_2 phase boundary at three different pressures, more high temperature crossings than in previous studies (e.g., Akins and Ahrens 2002; Nomura et al. 2010; Ono et al. 2002; Yamazaki et al. 2014). They also span a much wider range of pressures and temperatures, to better constrain this phase boundary while maintaining broad consistency with previous measurements.

The slope of our observed phase boundary is also significantly less steep than that calculated by Yang and Wu (2014), who reported a slope of 200(52) K/GPa (from Gibbs free energies) or 185(48) K/GPa (from shear instability), and that calculated by Tsuchiya et al. (2004), who found a slope of 167 K/GPa. Extrapolating this phase boundary to 0 K gives a transition pressure of 44 GPa, lower than that of most theoretical studies of SiO_2, which yield transition pressures of, for example, 46 GPa (Yang and Wu 2014), 47 GPa (Karki et al. 1997a), 53 GPa (Togo et al. 2008), 56 GPa (Tsuchiya et al. 2004), and 64 GPa (Lee and Gonze 1995). This may be due in part to possible curvature of the phase boundary at lower temperatures than those investigated here (Tsuchiya et al. 2004; Yang and Wu 2014).

4.2. Thermal equation of state of stishovite

These data were used to construct an equation of state for stishovite, relating its pressure, molar volume, and temperature. To ensure that the fitted equation of state would be compatible with the observed behavior of stishovite at ambient temperature, these data were first combined with those from several previous studies obtained at 300 K (Andrault et al. 2003; Grocholski et al. 2013; Hemley et al. 2000; Ross et al. 1990; Yamanaka et al. 2002) (Figure 4a). The primary criteria for choosing these studies from the many that exist in the literature is that they were all performed in a quasi-hydrostatic pressure medium: an alcohol mixture (Andrault et al. 2003; Ross et al. 1990; Yamanaka et al. 2002), neon (Grocholski et al. 2013), hydrogen (Hemley et al. 2000), or argon (Yamanaka et al. 2002), without any laser-annealing.

When combining datasets, it is important to give careful consideration to compatibility of the pressure standards. Hemley et al. (2000), Ross et al. (1990), and Yamanaka et al. (2000) all used ruby fluorescence to monitor the pressure in their experiments (Mao et al. 1986). Here their

pressures have been converted to the ruby scale of Dorogokupets and Oganov (2007), since the KBr pressure scale used in the present experiments was calibrated against the Pt scale of Dorogokupets and Oganov (2007). Grocholski et al. (2013) used gold as a pressure standard, and their pressures were recalculated using the gold equation of state of Dorogokupets and Oganov (2007). Andrault et al. (2003) used quartz as a pressure standard; their data were not corrected, but they were all obtained from pressures below 10 GPa, where most pressure scales are compatible.

A Mie-Grüneisen equation of state was fit to the combined dataset, in which the total pressure is described as the sum of an isothermal pressure, a harmonic thermal pressure (P_{TH}) term, and a quasi-anharmonic pressure (P_{AN}) term:

$$P(V,T) = P(V,300\text{K}) + [P_{TH}(V,T) - P_{TH}(V,300\text{K})] + [P_{AN}(V,T) - P_{AN}(V,300\text{K})] \quad (1)$$

The isothermal pressure term $P(V, 300\text{K})$ is given by the third-order Birch-Murnaghan equation of state (Birch 1952):

$$P(V,300K) = 3K_0 f(1+2f)^{\frac{5}{2}}\left(1+\frac{3}{2}(K_0'-4)f\right) \quad (2)$$

where K_0 is the isothermal bulk modulus, K_0' is its pressure derivative at constant temperature, $f = 0.5*[(V/V_0)^{-2/3} - 1]$ is the Eulerian strain, and the subscript 0 indicates values at 1 bar. The harmonic thermal pressure term in Eq. (1) can be derived from a Debye-type thermal energy (e.g., Dewaele et al. 2006):

$$P_{TH}(V,T) = \frac{9nR\gamma}{V}\left(\frac{\theta_D}{8} + T\left(\frac{T}{\theta_D}\right)^3 \int_0^{\theta_D/T} \frac{z^3 dz}{e^z - 1}\right) \quad (3)$$

where n is the number of atoms per formula unit, R is the ideal gas constant, $\gamma = \gamma_0(V/V_0)^q$ is the Grüneisen parameter, q is a constant describing the volume dependence of γ, and $\theta_D = \theta_0 \exp[(1-(V/V_0)^q)\ \gamma_0/q]$ is the Debye temperature. The quasi-anharmonic pressure term is fit as:

298 $$P_{AN}(V,T) = \frac{\gamma}{V} cT^2 \quad (4)$$

299 where c is a fitted constant. The T^2 dependence is derived from the lowest-order term of the high-
300 temperature expansion of the anharmonic free energy (Oganov and Dorogokupets 2004).

301 Since stishovite can be recovered as a metastable phase to ambient conditions, its
302 properties at 1 bar are well-characterized. Here a measured volume of 14.02 cm^3/mol was used
303 (Wang et al. 2012); this value is in agreement with those of most recent experimental studies
304 (e.g., Table 1). Recent Brillouin spectroscopy and ultrasonic interferometry measurements of
305 stishovite constrain its adiabatic bulk modulus at 1 bar to be 301–316 GPa (Brazhkin et al. 2005;
306 Jiang et al. 2009; Li et al. 1996; Yoneda et al. 2012) (Table 1). Here the value of 305 GPa was
307 used for the adiabatic K_0 from Li et al. (1996). The adiabatic (K_S) to isothermal (K_T) conversion
308 is given by $K_S = K_T(1+\alpha\gamma T)$, where α is the thermal expansion coefficient. Using T = 300 K, α =
309 1.647 x 10^{-5}/K from Nishihara et al. (2005), and the calculated γ_0 (see below), an isothermal K_0
310 of 302 GPa was calculated. The heat capacity (C_P) of stishovite at 1 bar was measured by Akaogi
311 et al. (2011), and the corresponding Debye temperature (θ_0) was calculated to be 1109 K (Akaogi
312 et al. 2011). Using these values for C_P, V_0, K_S, and α at one bar, the Grüneisen parameter can be
313 calculated as:

314 $$\gamma_0 = \frac{\alpha * K_S * V}{C_P} = 1.71 \quad (5)$$

315 Using this value for γ_0 along with the measured V_0 and K_{0T}, an unweighted nonlinear least-
316 squares minimization was used to fit Eqs. (1–4) to the combined stishovite dataset. Since fitting
317 q always resulted in a value of 1, a common approximation, q was fixed at 1 to determine K_0' and
318 c.

319 The resulting parameters are shown in Table 1, and isotherms calculated from this fit are
320 compared to the data in Figure 4a. Figure 4b shows the residuals to this fit, which range from –

4.2 GPa to +4.9 GPa. The root mean squared (rms) misfit in pressure is 1.8 GPa when considering only the data from this study, comparable to the 2σ uncertainty on the pressure measurements; the rms misfit is 1.6 GPa when considering all of the data in the fit. The covariance between K_0' and c is -0.0027×10^{-8}, corresponding to a correlation coefficient of $r = -0.74$, which reflects a significant anti-correlation between these two parameters in this fit. This equation of state is fit to data spanning up to 75 GPa and 300–3300 K, a significant advance over previous equations of state of stishovite, which reached a maximum pressure of 54 GPa (Wang et al. 2012) and maximum temperature of 2400 K (Pigott et al. 2015).

Table 1 compares our equation of state parameters to those of a variety of previous studies on stishovite. Table S1 includes equation of state parameters from a more exhaustive list of prior studies, reaching back as far as the 1960s. The fitted value of $K_0' = 5.24(9)$ agrees with a variety of previous studies within mutual 2σ uncertainties, including those based on ultrasonic interferometry at high pressures (Li et al. 1996), X-ray diffraction under static compression (Panero et al. 2003), dynamic compression (Luo et al. 2002a; Lyzenga et al. 1983), and theoretical calculations (Luo et al. 2002b). This result for K_0' is broadly consistent with other recent studies (e.g. Table 1) reporting that stishovite has a K_0' greater than the canonical value of 4 (Birch 1952). It falls above the values obtained in some recent studies (e.g., Table 1), which may be understood as a tradeoff between K_0 and K_0' (Supplemental Figure S1a). K_0 and K_0' are inversely correlated in literature studies of stishovite, and this fit agrees with the trend defined by previous studies (Supplemental Figure S1a). Prior studies have not resolved an anharmonic pressure term for stishovite, so comparisons to previous fits cannot be made.

4.3. Thermal equation of state of $CaCl_2$-type silica

Eqs. (1–4) have been similarly fit to the *P*-*V*-*T* data on $CaCl_2$-type silica to construct a thermal equation of state for this phase. As for stishovite, the data on the $CaCl_2$-type phase were combined with data obtained in previous studies at 300 K to ensure that the fit correctly captures the properties of this phase at ambient temperature. The data of Hemley et al. (2000) and Grocholski et al. (2013) were used and corrected to a common pressure scale (Section 4.2).

The $CaCl_2$-type phase of SiO_2 cannot be recovered to 1 bar, which makes fitting its thermal equation of state more challenging. To reduce the number of fitting parameters, which was necessary given the resolution of the data, the same V_0, θ_0, q, and c as for stishovite were used. The volumes predicted by the $CaCl_2$-type equation of state were also forced to match those of the stishovite equation of state at the phase boundary, since this transition is second-order with no accompanying volume change (e.g., Andrault et al. 2003). Again, a nonlinear least-squares minimization routine was used to determine K_0, K_0', and γ_0. The resulting parameters are listed in Table 2, and isotherms calculated from the fit are compared to the data in Figure 4a. The residuals to this fit are shown in Figure 4b, which span from –2.6 GPa to +3.1 GPa. The rms misfit in pressure is 1.5 GPa, or 1.4 GPa for the data in this study alone, comparable to the 2σ uncertainty on the pressure measurements. This is the first thermal equation of state of this phase determined in a diamond anvil cell; previously, its only thermal equation of state was based on a meta-analysis of shock wave data (Akins and Ahrens 2002). Here the quantity of equation of state data for this phase have been markedly increased, improving our understanding of its physical properties and its role in the Earth's interior.

Table 2 lists equation of state parameters for the $CaCl_2$-type phase from several previous studies. In comparison to other experimental studies (Andrault et al. 1998, 2003; Grocholski et al. 2013), a higher K_0 (341(4) GPa) and lower K_0' (3.20(16)) are reported here, though this is the

first study to report an experimentally-determined K_0' for this phase. This variability in measured parameters can be understood in terms of the strong tradeoff between K_0 and K_0' (Supplemental Figure S1b). If K_0' is fixed at 4 as in Andrault et al. (2003) and Grocholski et al. (2013), then K_0 = 321.8(11) GPa, in much better agreement with these studies. This fit (Table 2) indicates a correlation coefficient between K_0 and K_0' of r = –0.97 (Table S3), indicating that these parameters are almost perfectly inversely correlated. The Grüneisen parameter also exhibits moderate tradeoffs with the other fitted parameters, with an r = 0.45 with K_0 and r = –0.63 with K_0'. The fitted value of γ_0 = 2.14(4) is higher than that of Akins and Ahrens (2002) (1.4), who do not report an uncertainty on their fit but cover less of P-T space. In comparison to theoretical studies, this value for K_0 is significantly higher than that of Oganov et al. (2005) at 1 bar; at 50 GPa, the new equation of state yields K_T = 490 GPa, not far from the calculated values of Karki et al. (1997b) (509 GPa) and Yang and Wu (2014) (501–504 GPa) at this pressure.

Stishovite and the $CaCl_2$-type phase of silica have similar behavior under high pressures and temperatures, but with several differences in their properties that are resolved here. The $CaCl_2$-type structure has a higher K_0 than stishovite does (Tables 1–2), with a much lower value of K_0'. This results in the $CaCl_2$-type being more compressible at the phase boundary, and is reflected in the different curvatures of their isotherms (Figure 4a). At 49 GPa and 300 K, the isothermal bulk modulus of $CaCl_2$-type SiO_2 (487 GPa) is lower than that of stishovite (541 GPa). The γ_0 found for the $CaCl_2$-type phase is higher than that of stishovite for the same value of q, indicating that the $CaCl_2$-type has greater thermal expansivity.

4.4. Stishovite lattice parameter fits

The compressibility and thermal expansion of each axis of a tetragonal phase can be described independently using a pseudo-equation of state, replacing V with a^3 or c^3. Here a high-temperature third-order Birch-Murnaghan equation of state was used, to better facilitate comparisons with results of previous studies (e.g., Nishihara et al. 2005; Pigott et al. 2015). The high-temperature Birch-Murnaghan equation of state is identical to the regular Birch-Murnaghan equation of state (Eq. 2), except that the bulk modulus is replaced by:

$$K_0(T) = K_0(300K) + (T - 300K)\left(\frac{\partial K}{\partial T}\right) \quad (5)$$

and the 1 bar volume is replaced by:

$$V_0(T) = V_0(300K) * exp\left[\int_{300K}^{T} \alpha dT\right] \quad (6)$$

where α is the thermal expansion coefficient, approximated here as a constant (e.g., Angel 2001).

The 1 bar lattice parameters $a_0 = 4.178$ Å and $c_0 = 2.668$ Å were used for stishovite, as measured by Nishihara et al. (2005). Again the present data were pooled with those of several 300 K compression studies (Andrault et al. 2003; Grocholski et al. 2013; Hemley et al. 2000; Ross et al. 1990; Yamanaka et al. 2002), corrected to a common pressure scale (Section 4.2). For the a axis of stishovite, K_{0a}, K_{0a}', α_a, and $\partial K_{0a}/\partial T$ were fit (Table 3). A linear temperature dependence of α was found to be statistically insignificant. The a axis of stishovite is much more compressible than the bulk crystal ($K_{0a} = 269(4)$ GPa compared to $K_0 = 302$ GPa), with a lower K_0' ($K_{0a}' = 4.55(19)$ compared to $K_0' = 5.24(9)$). Figure 5 (upper panel) shows the raw data from this study and the previous studies used in the fit (Andrault et al. 2003; Grocholski et al. 2013; Hemley et al. 2000; Ross et al. 1990; Yamanaka et al. 2002), compared to calculated isotherms. The pressure residuals span a range of –3.6 GPa to +2.9 GPa (Supplemental Figure S2), with an rms misfit of 1.0 GPa. All of the parameters covary strongly with each other ($|r| > 0.6$), with the

strongest correlations between K_{0a} and K_{0a}' and between α_a and $\partial K_{0a}/\partial T$ (both $r = -0.95$) (Supplemental Table S4).

Table 3 also compares the lattice parameter fit for the stishovite *a* axis to results from previous studies, obtained using X-ray diffraction, Brillouin spectroscopy, and theoretical calculations. There is a remarkable degree of consensus on the compressibility of the *a* axis, with K_{0a} in the studies listed in Table 3 spanning the range 240(5)–284(5) GPa; the value found in this study, 269(4) GPa, falls in the middle of this range. The value of $\partial K_{0a}/\partial T = -0.020(2)$ GPa/K agrees well with that reported by Nishihara et al. (2005) (–0.023(4) GPa/K), and the value of $\alpha_a = 2.11(12) \times 10^{-5}$ K^{-1} matches those of Nishihara et al. (2005) ($2.06(14) \times 10^{-5}$ K^{-1}) and Wang et al. (2012) ($2.46(19) \times 10^{-5}$ K^{-1}) within mutual 2σ uncertainties, and is compatible with the thermal expansion expression of Pigott et al. (2015) at high temperatures.

The data from this study and literature data (Grocholski et al. 2013; Hemley et al. 2000) on the *c* axis of stishovite exhibit a much higher degree of scatter than those on the *a* axis (Figure 5, lower panel), as observed in previous studies (e.g., Nishihara et al. 2005). Therefore, in the lattice parameter fit for the stishovite *c* axis, K_{0c}' and $\partial K_{0c}/\partial T$ were held fixed to the values found for the *a* axis (Table 3), and K_{0c} and α_c were fit (Table 3). Isotherms calculated from the fit are compared to the data in Figure 5 (lower panel). The pressure residuals range from –10.1 GPa to +13.6 GPa (Supplemental Figure S3), and the fit has an rms misfit in pressure of 4.5 GPa. K_{0c} and α_c have a correlation coefficient $r = -0.93$.

Previous experimental studies on the *c* axis of stishovite have reported K_{0c} values spanning 411–556 GPa. The value of 435(9) GPa reported here falls within this range, agreeing within mutual 2σ uncertainties with values reported previously using X-ray diffraction (Liu et al. 1999; Nishihara et al. 2005; Pigott et al. 2015), which tend to be lower than values reported using

Brillouin spectroscopy (Jiang et al. 2009; Weidner et al. 1982) and computational results (Cohen 1991). The value of $\alpha_c = 1.70(11) \times 10^{-5}$ K^{-1} falls intermediate between those reported previously by Nishihara et al. (2005) and Wang et al. (2012), agreeing with both of these values within mutual 2σ uncertainties, and also agrees well with the expression of Pigott et al. (2015) for thermal expansion at high temperatures. The *c* axis of stishovite exhibits a lower thermal expansion than the *a* axis by 19%, as reported previously (Table 3). It is more incompressible than the bulk crystal (K_{0c} = 435(9) GPa), and significantly (62%) more incompressible than the *a* axis, an effect that has also been reported previously (Table 3). The higher compressibility of the *a* axis has been attributed to a greater degree of flexibility in the corner-sharing linkages of SiO_6 octahedra along the *a* axis, as opposed to the stiffer edge-sharing linkages along the *c* axis (Nishihara et al. 2005).

The axial *c*/*a* ratio of stishovite can be calculated from our lattice parameter fits (Supplemental Figure S4). The *c*/*a* ratio of stishovite increases approximately linearly with decreasing volume, by ~0.0057 per cm^3/mol. The temperature effect on the *c*/*a* ratio is not apparent from the data given the measurement uncertainties, which are large relative to the observed variations in *c*/*a* (variation of only ~1.5% over the range of conditions in this study).

To evaluate internal consistency, volumes calculated from the equation of state of stishovite were compared to volumes calculated as $V = a^2c$ from the lattice parameter fits for the *a* and *c* axes. Supplemental Figure S5 shows the misfit between these volumes as a function of volume for temperatures of 300–3500 K over the entire pressure range of stishovite stability (Shen and Lazor 1995; Zhang et al. 1996) (Figure 3). It reaches a maximum of ~0.5% misfit in volume at 2500 K and low pressures, but is less than ~0.1% over most of the range of conditions investigated (less than uncertainties on most measured volumes). The fits of the *a* and *c* axes

457 slightly overestimate the volume at lower volumes (up to ~13.5 cm^3/mol) and underestimate the
458 volume at higher volumes.

459 Just beyond the transition pressure, the *a* axis of the $CaCl_2$-type phase expands and the *b*
460 axis shrinks (Supplemental Figure S6) (e.g., Andrault et al. 2003; Hemley et al. 2000); this
461 behavior precludes a simple fit for the $CaCl_2$-type lattice parameters as was done here for
462 stishovite. A much smaller splitting between the *a* and *b* axes was observed here than in previous
463 studies at 300 K (Grocholski et al. 2013; Hemley et al. 2000). This difference does not appear to
464 be a thermal effect, since both axes expand with increasing temperature, such that the difference
465 between them is approximately independent of temperature. It may be due to the more
466 hydrostatic conditions of this study caused by the high temperatures at which the data were
467 collected (Section 3). The data from this study on the *c* axis of the $CaCl_2$-type phase are
468 compatible with those of previous studies at 300 K (Grocholski et al. 2013; Hemley et al. 2000),
469 and shows a higher compressibility than the *c* axis of stishovite at these conditions (Figure S6).
470

471 **4.5. SiO_2 in the deep Earth**

472 It has been demonstrated experimentally that free silica is one of the phases that forms
473 when mid-ocean ridge basalt (MORB) compositions are subjected to the pressures and
474 temperatures of Earth's lower mantle, which may occur in subducting slabs. For example, at 40–
475 60 GPa and 2100 K, a MORB composition has been shown to contain 15–19 wt% stishovite
476 (Hirose et al. 2005; Perrillat et al. 2006; Ricolleau et al. 2010). Subducted continental crust likely
477 contains an even higher proportion of free silica (e.g., Irifune et al. 1994; Ishii et al. 2012). Due
478 to its abundance in these geological settings, it is important to consider the density of SiO_2 at
479 lower mantle conditions.

Figure 6 shows the density of SiO_2 at the *P*-*T* conditions of the Earth's transition zone and lower mantle. Along a mantle geotherm (Brown and Shankland 1981), the phase transition from stishovite to $CaCl_2$-type SiO_2 occurs at a pressure of 78 GPa, or a depth of 1840 km. Two possible slab temperature profiles were also considered, a "hot slab" that is 200 K cooler than the mantle geotherm and a "cold slab" that is 600 K cooler (e.g., Syracuse et al. 2010). These lower temperatures increase the density of SiO_2, and push the phase transition to lower pressures (75 GPa in a hot slab and 68 GPa in a cold slab). The minimum temperature inside the slab can be ~100–500 K cooler than the slab surface (e.g., Syracuse et al. 2010); any silica present in the interior of a slab could therefore have a slightly higher density and lower transition pressure than considered here. Figure 6 also shows the density profile of the Earth from the Preliminary Reference Earth Model, PREM (Dziewonski and Anderson 1981). Along a mantle geotherm, silica is denser than the surrounding mantle to a pressure of 58 GPa, or a depth of 1420 km, and is less dense than the mantle at greater depths. In a cold slab, silica is denser than the mantle up to 68 GPa or 1640 km. At greater depths in the Earth (124–128 GPa or 2690–2770 km, depending on temperature), the $CaCl_2$-type silica will transform to seifertite (Grocholski et al. 2013).

5. Implications

A thermal equation of state has been constructed for stishovite that extends to significantly higher pressures and temperatures than previous studies (e.g., Pigott et al. 2015; Wang et al. 2012), and the first thermal equation of state of $CaCl_2$-type silica measured in a laser-heated diamond anvil cell is reported (Figure 4), greatly improving the pressure and temperature coverage for this phase. This *P*-*T* coverage makes these equations of state more

accurate and less prone to errors in extrapolation when applying them to understanding the deep Earth.

Free silica is unlikely to be present in a pyrolitic lower mantle, but may occur in a subducting slab (e.g., Hirose et al. 2005). Based on measurements of the phase boundary between stishovite and $CaCl_2$-type SiO_2 (Figure 3), this phase transition should occur at pressures of 68–78 GPa in the Earth's lower mantle, with uncertainty due to temperature. Because this transition is second-order with no discontinuity in density, it is unlikely that it would be observable as a seismological reflection, though it may be detectable based on seismic velocities and anisotropy (e.g., Yang and Wu 2014). However, it is important to know the depth of this transition in modeling the density of silica in the Earth, because these two phases have different compressibilities and thermal properties (Tables 1–2). Silica is denser than the surrounding mantle up to pressures of 58–68 GPa, or depths of 1420–1640 km, depending on temperature. At shallower depths, silica can contribute to the gravitational force pulling on a sinking slab. At greater depths, silica is less dense than the mantle, providing a source of buoyancy to resist the downward motion of the slab. It has recently been suggested that SiO_2 may exsolve from the core as it cools (Hirose et al. 2017). Silica entering the lower mantle this way will tend to ascend buoyantly until it is consumed by the SiO_2-undersaturated mantle.

Acknowledgments

We are grateful to the editor for handling our manuscript and to two anonymous reviewers for their constructive feedback. We thank Dion Heinz, Jacob Britz, and beamline scientist Clemens Prescher for assistance with running experiments. This work was supported by a National Science Foundation (NSF) Graduate Research Fellowship, Illinois Space Grant

Consortium Graduate Research Fellowship, International Centre for Diffraction Data Ludo Frevel Crystallography Scholarship, University of Chicago Plotnick Fellowship, and NSF Postdoctoral Fellowship (EAR-1452626) to RAF and NSF grant EAR-1427123 to AJC. JSP was supported by the OSU Presidential Fellowship and NSF grant EAR-0955647 awarded to Wendy R. Panero and would like to thank CDAC for the HPCAT beamtime award. JSS acknowledges the support of DOE-BES/DMSE under Award DE-FG02-99ER45775. Portions of this work were performed at GeoSoilEnviroCARS (Sector 13), Advanced Photon Source (APS), Argonne National Laboratory (ANL). GeoSoilEnviroCARS is supported by the NSF – Earth Sciences (EAR-1634415) and the Department of Energy (DOE) – Geosciences (DE-FG02-94ER14466). Portions of this work were performed at HPCAT (Sector 16), APS, ANL. HPCAT operation is supported by DOE-NNSA under Award No. DE-NA0001974, with partial instrumentation funding by NSF. This research used resources of the APS, a U.S. DOE Office of Science User Facility operated for the DOE Office of Science by ANL under Contract No. DE-AC02-06CH11357.

References

Akins, J.A., and Ahrens, T.J. (2002) Dynamic compression of SiO_2: A new interpretation. Geophysical Research Letters, 29, 1394.

Akaogi, M., Oohata, M., Kojitani, H., and Kawaji, H. (2011) Thermodynamic properties of stishovite by low-temperature heat capacity measurements and the coesite-stishovite transition boundary. American Mineralogist, 96, 1325–1330.

Andrault, D., Fiquet, G., Guyot, F., and Hanfland, M. (1998) Pressure-induced Landau-type transition in stishovite. Science, 282, 720–724.

549 Andrault, D., Angel, R.J., Mosenfelder, J.L., and Le Bihan, T. (2003) Equation of state of
550 stishovite to lower mantle pressures. American Mineralogist, 88, 301–307.
551 Angel, R.J. (2000) Equations of state. Reviews in Mineralogy and Geochemistry, 41, 35–59.
552 Asahara, Y., Hirose, K., Ohishi, Y., Hirao, N., Ozawa, H., and Murikami, M. (2013) Acoustic
553 velocity measurements for stishovite across the post-stishovite phase transition under
554 deviatoric stress: Implications for the seismic features of subducting slabs in the mid-mantle.
555 American Mineralogist, 98, 2053–2062.
556 Birch, F. (1952) Elasticity and constitution of the Earth's interior. Journal of Geophysical
557 Research, 57, 227–286.
558 Brazhkin, V.V., McNeil, L.E., Grimsditch, M., Bendeliani, N.A., Dyuzheva, T.I., and Lityagina,
559 L.M. (2005) Elastic constants of stishovite up to its amorphization temperature. Journal of
560 Physics: Condensed Matter, 17, 1869–1875.
561 Brown, J.M., and Shankland, T.J. (1981) Thermodynamic parameters in the Earth as determined
562 from seismic profiles. Geophysical Journal of the Royal Astronomical Society, 66, 579–596.
563 Campbell, A.J., Seagle, C.T., Heinz, D.L., Shen, G., and Prakapenka, V.B. (2007) Partial melting
564 in the iron–sulfur system at high pressure: A synchrotron X-ray diffraction study. Physics of
565 the Earth and Planetary Interiors, 162, 119–128.
566 Campbell, A.J., Danielson, L., Righter, K., Seagle, C.T., Wang, Y., and Prakapanka, V.B. (2009)
567 High pressure effects on the iron–iron oxide and nickel–nickel oxide oxygen fugacity
568 buffers. Earth and Planetary Science Letters, 286, 556–564.
569 Chao, E.C.T., Fahey, J.J., Littler, J., and Milton, D.J. (1962) Stishovite, SiO_2, a very high
570 pressure new mineral from Meteor Crater, Arizona. Journal of Geophysical Research, 67,
571 419–421.

572 Cohen, R.E. (1991) Bonding and elasticity of stishovite SiO_2 at high pressure: Linearized
573 augmented plane wave calculations. American Mineralogist, 76, 733–742.
574 Dewaele, A., Loubeyre, P., Occelli, F., Mezouar, M., Dorogokupets, P.I., and Torrent, M. (2006)
575 Quasihydrostatic equation of state of iron above 2 Mbar. Physical Review Letters, 97,
576 215504.
577 Dorfman, S.M., Prakapenka, V.B., Meng, Y., amd Duffy, T.S. (2012) Intercomparison of
578 pressure standards (Au, Pt, Mo, MgO, NaCl and Ne) to 2.5 Mbar. Journal of Geophysical
579 Research, 117, B08210.
580 Dorogokupets, P.I., and Oganov, A.R. (2007) Ruby, metals, and MgO as alternative pressure
581 scales: A semiempirical description of shock-wave, ultrasonic, x-ray, and thermochemical
582 data at high temperatures and pressures. Physical Review B, 75, 024115.
583 Driver, K.P., Cohen, R.E., Wu, Z., Militzer, B., López Ríos, P., Towler, M.D., Needs, R.J., and
584 Wilkins, J.W. (2010) Quantum Monte Carlo computations of phase stability, equations of
585 state, and elasticity of high-pressure silica. Proceedings of the National Academy of Sciences
586 of the United States of America, 107, 9519–9524.
587 Dubrovinsky, L.S., Saxena, S.K., Lazor, P., Ahuja, R., Eriksson, O., Wills, J.M., and Johansson,
588 B. (1997) Experimental and theoretical identification of a new high-pressure phase of silica.
589 Nature, 388, 362–365.
590 Dubrovinsky, L.S., Dubrovinskaia, N.A., Prakapenka, V., Seifert, F., Langenhorst, F., Dmitriev,
591 V., Weber, H.-P., and Le Bihan, T. (2003) High-pressure and high-temperature
592 polymorphism in silica. High Pressure Research, 23, 35–39.
593 Dziewonski, A.M., and Anderson, D.L. (1981) Preliminary reference Earth model. Physics of the
594 Earth and Planetary Interiors, 25, 297–356.

595 Fischer, R.A., Campbell, A.J., Shofner, G.A., Lord, O.T., Dera, P., and Prakapenka, V.B. (2011)
596 Equation of state and phase diagram of FeO. Earth and Planetary Science Letters, 304, 496–
597 502.
598 Fischer, R.A., Campbell, A.J., Caracas, R., Reaman, D.M., Dera, P., and Prakapenka, V.B.
599 (2012) Equation of state and phase diagram of Fe–16Si alloy as a candidate component of
600 Earth's core. Earth and Planetary Science Letters, 357–358, 268–276.
601 Fischer, R.A., Campbell, A.J., Caracas, R., Reaman, D.M., Heinz, D.L., Dera, P., and
602 Prakapenka, V.B. (2014) Equations of state in the Fe–FeSi system at high pressures and
603 temperatures. Journal of Geophysical Research: Solid Earth, 119, 2810–2827.
604 Fischer, R.A., Nakajima, Y., Campbell, A.J., Frost, D.J., Harries, D., Langenhorst, F., Miyajima,
605 N., Pollok, K., and Rubie, D.C. (2015) High pressure metal–silicate partitioning of Ni, Co, V,
606 Cr, Si, and O. Geochimica et Cosmochimica Acta, 167, 177–194.
607 Grocholski, B., Shim, S.-H., and Prakapenka, V.B. (2013) Stability, metastability, and elastic
608 properties of a dense silica polymorph, seifertite. Journal of Geophysical Research: Solid
609 Earth, 118, 1–13.
610 Haines, J., Léger, J.M., Gorelli, F., and Hanfland, M. (2001) Crystalline post-quartz phase in
611 silica at high pressure. Physical Review Letters, 87, 155503.
612 Hammersley, A.P., Svensson, S.O., Hanfland, M., Fitch, A.N., and Häusermann, D. (1996) Two-
613 dimensional detector software: From real detector to idealised image or two-theta scan. High
614 Pressure Research, 14, 235–248.
615 Hazen, R.M., Finger, L.W., Hemley, R.J., and Mao, H.K. (1989) High-pressure crystal chemistry
616 and amorphization of α-quartz. Solid State Communications, 72, 507–511.

Hemley, R.J. (1987) Pressure dependence of Raman spectra of SiO_2 polymorphs: α-quartz, coesite, and stishovite. In: M.H. Manghnani and Y. Syono, Eds., High-Pressure Research in Mineral Physics, pp. 347–359. Terra Scientific Publishing Company, Tokyo, Japan / American Geophysical Union, Washington, D.C., U.S.A.

Hemley, R.J., Shu, J., Carpenter, M.A., Hu, J., Mao, H.K., and Kingma, K.J. (2000) Strain/order parameter coupling in the ferroelastic transition in dense SiO_2. Solid State Communications, 114, 527–532.

Hirose, K., Takafuji, N., Sata, N., and Ohishi, Y. (2005) Phase transition and density of subducted MORB crust in the lower mantle. Earth and Planetary Science Letters, 237, 239–251.

Hirose, K., Morard, G., Sinmyo, R., Umemoto, K., Hernlund, J., Helffrich, G., and Lebrosse, S. (2017) Crystallization of silicon dioxide and compositional evolution of the Earth's core. Nature, 543, 99–102.

Irifune, T., Ringwood, A.E., and Hibberson, W.O. (1994) Subduction of continental crust and terrigenous and pelagic sediments: An experimental study. Earth and Planetary Science Letters, 126, 351–368.

Ishii, T., Kojitani, H., and Akaogi, M. (2012) High-pressure phase transitions and subduction behavior of continental crust at pressure-temperature conditions up to the upper part of the lower mantle. Earth and Planetary Science Letters, 357–358, 31–41.

Jiang, F., Gwanmesia, G.D., Dyuzheva, T.I., and Duffy, T.S. (2009) Elasticity of stishovite and acoustic mode softening under high pressure by Brillouin scattering. Physics of the Earth and Planetary Interiors, 172, 235–240.

639 Karki, B.B., Warren, M.C., Stixrude, L., Ackland, G.J., and Crain, J. (1997a) *Ab initio* studies of
640 high-pressure structural transformations in silica. Physical Review B, 55, 3465–3471.
641 Karki, B.B., Stixrude, L., and Crain, J. (1997b) Ab initio elasticity of three high-pressure
642 polymorphs of silica. Geophysical Research Letters, 24, 3269–3272.
643 Kingma, K.J., Hemley, R.J., Mao, H.-k., and Veblen, D.R. (1993) New high-pressure
644 transformations in α-quartz. Physical Review Letters, 70, 3927–3930.
645 Kingma, K.J., Cohen, R.E., Hemley, R.J., and Mao, H.-k. (1995) Transformation of stishovite to
646 a denser phase at lower-mantle pressures. Nature, 374, 243–245.
647 Komabayashi, T., and Fei, Y. (2010) Internally consistent thermodynamic database for iron to
648 the Earth's core conditions. Journal of Geophysical Research, 115, B03202.
649 Lakshtanov, D.L., Sinogeikin, S.V., Litasov, K.D., Prakapenka, V.B., Hellwig, H., Wang, J.,
650 Sanches-Valle, C., Perrillat, J.-P., Chen, B., Somayazulu, M., Li, J., Ohtani, E., and Bass,
651 J.D. (2007) The post-stishovite phase transition in hydrous alumina-bearing SiO_2 in the lower
652 mantle of the earth. Proceedings of the National Academy of Sciences of the United States of
653 America, 104, 13588–13590.
654 Lee, C., and Gonze, X. (1995) The pressure-induced ferroelastic phase transition of SiO_2
655 stishovite. Journal of Physics: Condensed Matter, 7, 3693–3698.
656 Li, B., Rigden, S.M., and Liebermann, R.C. (1996) Elasticity of stishovite at high pressure.
657 Physics of the Earth and Planetary Interiors, 96, 113–127.
658 Liu, J., Zhang, J., Flesch, L., Li, B., Weidner, D.J., and Liebermann, R.C. (1999) Thermal
659 equation of state of stishovite. Physics of the Earth and Planetary Interiors, 112, 257–266.

660 Luo, S.-N., Mosenfelder, J.L., Asimow, P.D., and Ahrens, T.J. (2002a) Direct shock wave
661 loading of stishovite to 235 GPa: Implications for perovskite stability relative to an oxide
662 assemblage at lower mantle conditions. Geophysical Research Letters, 29, 1691.
663 Luo, S.-N., Çağin, T., Strachan, A., Goddard, W.A. III, and Ahrens, T.J. (2002b) Molecular
664 dynamics modeling of stishovite. Earth and Planetary Science Letters, 202, 147–157.
665 Lyzenga, G.A., Ahrens, T.J., and Mitchell, A.C. (1983) Shock temperatures of SiO_2 and their
666 geophysical implications. Journal of Geophysical Research, 88, 2431–2444.
667 Mao, H.K., Xu, J., and Bell, P.M. (1986) Calibration of the ruby pressure gauge to 800 kbar
668 under quasi-hydrostatic conditions. Journal of Geophysical Research, 91, 4673–4676.
669 Meng, Y., Hrubiak, R., Rod, E., Boehler, R., and Shen, G. (2015) New developments in laser-
670 heated diamond anvil cell with *in situ* synchrotron x-ray diffraction at High Pressure
671 Collaborative Access Team. Review of Scientific Instruments, 86, 072201.
672 Murakami, M., Hirose, K., Ono, S., and Ohishi, Y. (2003) Stability of $CaCl_2$-type and α-PbO_2-
673 type SiO_2 at high pressure and temperature determined by in-situ X-ray measurements.
674 Geophysical Research Letters, 30, 1207.
675 Nishihara, Y., Nakayama, K., Takahashi, E., Iguchi, T., and Funakoshi, K.-i. (2005) *P-V-T*
676 equation of state of stishovite to the mantle transition zone conditions. Physics and Chemistry
677 of Minerals, 31, 660–670.
678 Nomura, R., Hirose, K., Sata, N., and Ohishi, Y. (2010) Precise determination of post-stishovite
679 phase transition boundary and implications for seismic heterogeneities in the mid–lower
680 mantle. Physics of the Earth and Planetary Interiors, 183, 104–109.
681 Oganov, A.R., and Dorogokupets, P.I. (2004) Intrinsic anharmonicity in equations of state and
682 thermodynamics of solids. Journal of Physics: Condensed Matter, 16, 1351–1360.

683 Oganov, A.R., Gillan, M.J., and Price, G.D. (2005) Structural stability of silica at high pressures
684 and temperatures. Physical Review B, 71, 064104.
685 Ono, S., Hirose, K., Murakami, M., and Isshiki, M. (2002) Post-stishovite phase boundary in
686 SiO_2 determined by in situ X-ray observations. Earth and Planetary Science Letters, 197,
687 187–192.
688 Panero, W.R., Benedetti, L.R., and Jeanloz, R. (2003) Equation of state of stishovite and
689 interpretation of SiO_2 shock-compression data. Journal of Geophysical Research, 108, 2015.
690 Perrillat, J.-P., Ricolleau, A., Daniel, I., Fiquet, G., Mezouar, M., Guignot, N., and Cardon, H.
691 (2006) Phase transformations of subducted basaltic crust in the upmost lower mantle. Physics
692 of the Earth and Planetary Interiors, 157, 139–149.
693 Pigott, J.S., Ditmer, D.A., Fischer, R.A., Reaman, D.M., Hrubiak, R., Meng, Y., Davis, R.J., and
694 Panero, W.R. (2015) High-pressure, high-temperature equations of state using nanofabricated
695 controlled-geometry Ni/SiO_2/Ni double hot-plate samples. Geophysical Research Letters, 42,
696 10239–10247.
697 Prakapenka, V.B., Shen, G., Dubrovinsky, L.S., Rivers, M.L., and Sutton, S.R. (2004) High
698 pressure induced phase transformation of SiO_2 and GeO_2: Difference and similarity. Journal
699 of Physics and Chemistry of Solids, 65, 1537–1545.
700 Prakapenka, V.B., Kubo, A., Kuznetsov, A., Laskin, A., Shkurikhin, O., Dera, P., Rivers, M.L.,
701 and Sutton, S.R. (2008) Advanced flat top laser heating system for high pressure research at
702 GSECARS: Application to the melting behavior of germanium. High Pressure Research, 28,
703 225–235.

Prescher, C., and Prakapenka, V.B. (2015) DIOPTAS: A program for reduction of two-dimensional X-ray diffraction data and data exploration. High Pressure Research, 35, 223–230.

Ricolleau, A., Perrillat, J.-P., Fiquet, G., Daniel, I., Matas, J., Addad, A., Menguy, N., Cardon, H., Mezouar, M., and Guignot, N. (2010) Phase relations and equation of state of a natural MORB: Implications for the density profile of subducted oceanic crust in the Earth's lower mantle. Journal of Geophysical Research, 115, B08202.

Ross, N.L., Shu, J.-F., Hazen, R.M., and Gasparik, T. (1990) High-pressure crystal chemistry of stishovite. American Mineralogist, 75, 739–747.

Shen, G., and Lazor, P. (1995) Measurement of melting temperature of some minerals under lower mantle pressures. Journal of Geophysical Research, 100, 17699–17713.

Shen, G., Rivers, M.L., Wang, Y., and Sutton, S.R. (2001) Laser heated diamond anvil cell system at the Advanced Photon Source for *in situ* X-ray measurements at high pressure and temperature. Review of Scientific Instruments, 72, 1273–1282.

Shen, G., Prakapenka, V.B., Eng, P.J., Rivers, M.L., and Sutton, S.R. (2005) Facilities for high-pressure research with the diamond anvil cell at GSECARS. Journal of Synchrotron Radiation, 12, 642–649.

Shieh, S.R., Duffy, T.S., and Shen, G. (2005) X-ray diffraction study of phase stability in SiO_2 at deep mantle conditions. Earth and Planetary Science Letters, 235, 273–282.

Syracuse, E.M., van Keken, P.E., and Abers, G.A. (2010) The global range of subduction zone thermal models. Physics of the Earth and Planetary Interiors, 183, 73–90.

Togo, A., Oba, F., and Tanaka, I. (2008) First-principles calculations of the ferroelastic transition between rutile-type and $CaCl_2$-type SiO_2 at high pressures. Physical Review B, 78, 134106.

Tsuchida, Y., and Yagi, T. (1989) A new, post-stishovite high-pressure polymorph of silica. Nature, 340, 217–220.

Tsuchida, Y., and Yagi, T. (1990) New pressure-induced transformations of silica at room temperature. Nature, 347, 267–269.

Tsuchiya, T., Caracas, R., and Tsuchiya, J. (2004) First principles determination of the phase boundaries of high-pressure polymorphs of silica. Geophysical Research Letters, 31, L11610.

Tsuno, K., Frost, D.J., and Rubie, D.C. (2013) Simultaneous partitioning of silicon and oxygen into the Earth's core during early Earth differentiation. Geophysical Research Letters, 40, 66–71.

Wang, F., Tange, Y., Irifune, T., and Funakoshi, K.-i. (2012) *P*-*V*-*T*- equation of state of stishovite up to mid-lower mantle conditions. Journal of Geophysical Research, 117, B06209.

Weidner, D.J., Bass, J.D., Ringwood, A.E., and Sinclair, W. (1982) The single-crystal elastic moduli of stishovite. Journal of Geophysical Research, 87, 4740–4746.

Yamanaka, T., Fukuda, T., and Tsuchiya, J. (2002) Bonding character of SiO_2 stishovite under high pressures up to 30 GPa. Physics and Chemistry of Minerals, 29, 633–641.

Yamazaki, D., Ito, E., Yoshino, T., Tsujino, N., Yoneda, A., Guo, X., Xu, F., Higo, Y., and Funakoshi, K. (2014) Over 1 Mbar generation in the Kawai-type multianvil apparatus and its application to compression of $(Mg_{0.92}Fe_{0.08})SiO_3$ perovskite and stishovite. Physics of the Earth and Planetary Interiors, 228, 262–267.

Yang, R., and Wu, Z. (2014) Elastic properties of stishovite and the $CaCl_2$-type silica at the mantle temperature and pressure: An ab initio investigation. Earth and Planetary Science Letters, 404, 14–21.

Yoneda, A., Corray, T., and Shatskiy, A. (2012) Single-crystal elasticity of stishovite: New experimental data obtained using high-frequency resonant ultrasound spectroscopy and a Gingham check structure model. Physics of the Earth and Planetary Interiors, 190–191, 80–86.

Zhang, J., Li, B., Utsumi, W., and Liebermann, R.C. (1996) In situ X-ray observations of the coesite–stishovite transition: Reversed phase boundary and kinetics. Physics and Chemistry of Minerals, 23, 1–10.

Figure captions

Figure 1: Previous results on the phase transition from stishovite to $CaCl_2$-type SiO_2, compared to the phase boundary found in this study. Top: phase boundary at high temperatures. Filled grey hexagons: observations of stishovite. Open grey pentagons: observations of the $CaCl_2$-type structure. Phase boundary from this study is from Figure 3. Bottom: transition pressures measured or calculated at room temperature. Result from Wang et al. (2012) is a lower bound. Results from Hemley et al. (2000) were obtained on either compression (higher pressure) or decompression (lower pressure).

Figure 2: X-ray diffraction patterns of SiO_2. (a) Representative pattern from 74(2) GPa and 2160(120) K. All peaks correspond to B2-KBr, stishovite, or platinum, with one reflection from the rhenium gasket. Black rectangle indicates region enlarged in part (b). Inset: 2D diffraction image before integration. Yellow arrow indicates region enlarged in part (b). (b) Splitting of the stishovite 301 peak into the $CaCl_2$-type 301 and 031 peaks across the phase transition as a function of temperature. Patterns were collected on cooling at ~74 GPa. Yellow pattern is from

part (a). Patterns are offset vertically for clarity. The stishovite 301 peak splits between 2160(120) K and 1870(110) K, bracketing the phase transition. Insets: Fixed location in the lower left quadrant of the 2D diffraction images from 2160 K (upper) and 1870 K (lower), showing the splitting of a single 301/031 reflection. Image encompasses a 2θ range of ~0.5º. Temperature uncertainties are 110–180 K.

Figure 3: Phase diagram results on silica. Filled orange circles: observations of the stishovite structure. Open green circles: $CaCl_2$-type structure.

Figure 4: Pressure-volume-temperature data and equation of state fits (Tables 1–2) for stishovite and $CaCl_2$-type SiO_2 (a), and residuals to these fits (b). Curves in (a) are isotherms calculated for the midpoint of the indicated temperature ranges. Solid curves and filled symbols: stishovite. Dashed curves and open symbols: $CaCl_2$-type SiO_2. Curves in (a) are truncated at the edge of the stability fields of the phases (Grocholski et al. 2013; Shen and Lazor 1995; Zhang et al. 1996) (Figure 3), but some metastable data are shown. Circles: this study. Diamonds: Hemley et al. (2000). Squares: Grocholski et al. (2013). Upward-pointing triangles: Ross et al. (1990). Right-pointing triangles: Andrault et al. (2003). Left-pointing triangles: Yamanaka et al. (2002). Horizontal and vertical error bars in (b) are both uncertainties in measured pressure. Data have been corrected to a common pressure scale.

Figure 5: Pressure-lattice parameter-temperature data and fits (Table 3) for the *a* axis (upper panel) and *c* axis (lower panel) of stishovite. Curves are isotherms calculated for the midpoint of the indicated temperature ranges, and are truncated at the edge of the stability field of stishovite

(Shen and Lazor 1995; Zhang et al. 1996) (Figure 3), but some metastable data are shown. Symbols are as in Figure 4. Data have been corrected to a common pressure scale. Residuals to these fits are shown in Supplemental Figures S2–S3.

Figure 6: Density of SiO_2 in Earth's transition zone and lower mantle calculated from the equations of state of this study (Tables 1–2) for different temperature profiles, compared to PREM (Dziewonski and Anderson 1981). Solid curves: stishovite. Dashed curves: $CaCl_2$-type SiO_2. Density of the stable phase is plotted, according to the phase boundary in Figure 3. Mantle geotherm is from Brown and Shankland (1981); hot and cold slab temperatures are 200 K and 600 K cooler, respectively (e.g., Syracuse et al. 2010). Pressure-depth relationship is from Dziewonski and Anderson (1981).

Table captions

Table 1: Equation of state parameters for stishovite, from this study and a selection of previous studies. Equation of state parameters are as defined in the text for 1 bar and 300 K, and all bulk moduli are isothermal, unless otherwise noted. Entries in *italics* were held fixed in the fits. Stated uncertainties for this study do not incorporate covariance between terms. For more stishovite equations of state from the literature, see Supplemental Table S1.

Table 2: Equation of state parameters for the $CaCl_2$-type phase of silica, from this study and previous studies. Equation of state parameters are as defined in the text for 1 bar and 300 K, and all bulk moduli are isothermal. Entries in *italics* were held fixed in the fits. Stated uncertainties

for this study do not incorporate covariance between terms; the variance-covariance matrix for this fit is shown in Supplemental Table S3.

Table 3: Lattice parameter fits for the *a* and *c* axes of stishovite, from this study and a selection of previous studies. Entries in *italics* were held fixed in the fits. Stated uncertainties for this study do not incorporate covariance between terms; the variance-covariance matrix for the *a* axis fit is shown in Supplemental Table S4.

Study	K_{0a} (GPa)	K_{0a}'	$\partial K_{0a}/\partial T$ (GPa/K)	$_a$ (K^{-1})
This study	269(4)	4.55(19)	–0.020(2)	$2.11(12) \times 10^{-5}$
Andrault et al. (2003)	250.9(16)	5.48(32)		
Liu et al. (1999)	269(9)			
Nishihara et al. (2005)	240(5)	6.2(5)	–0.023(4)	$2.06(14) \times 10^{-5}$
Pigott et al. (2015)	284(5)	*4*	–0.050(3)	
Wang et al. (2012)				$2.46(19) \times 10^{-5}$
Jiang et al. (2009)	256			
Weidner et al. (1982)	253			
Cohen (1991)	262			

K_{0c} (GPa)	K_{0c}'	$\partial K_{0c}/\partial T$ (GPa/K)	$_c$ (K^{-1})	Method
435(9)	*4.55*	*-0.020*	$1.70(11) \times 10^{-5}$	XRD
				XRD
513(32)				XRD
411(9)	*4*	–0.036(21)	$1.22(24) \times 10^{-5}$	XRD
450(20)	*4*	–0.091(7)		XRD
			$1.87(20) \times 10^{-5}$	XRD
521				Brillouin
556				Brillouin
615				calculated

Figure 1

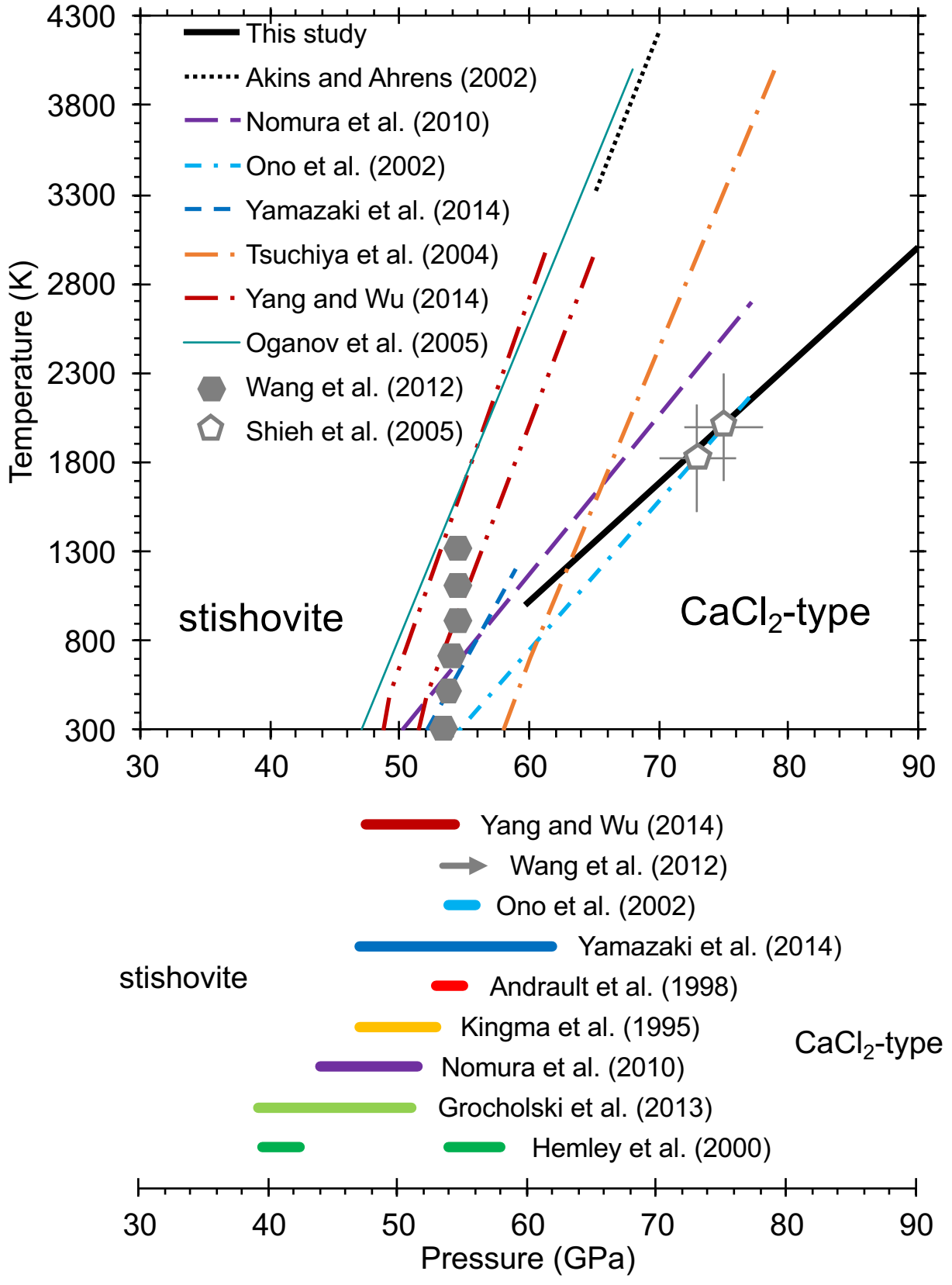
This study
Akins and Ahrens (2002)
Nomura et al. (2010)
Ono et al. (2002)
Yamazaki et al. (2014)
Tsuchiya et al. (2004)
Yang and Wu (2014)
Oganov et al. (2005)
Wang et al. (2012)
Shieh et al. (2005)
stishovite
CaCl2-type
Temperature (K)
4300
3800
3300
2800
2300
1800
1300
800
300
30
40
50
60
70
80
90
Yang and Wu (2014)
Wang et al. (2012)
Ono et al. (2002)
Yamazaki et al. (2014)
Andrault et al. (1998)
Kingma et al. (1995)
Nomura et al. (2010)
Grocholski et al. (2013)
Hemley et al. (2000)
stishovite
CaCl2-type
Pressure (GPa)

Figure 2(a)

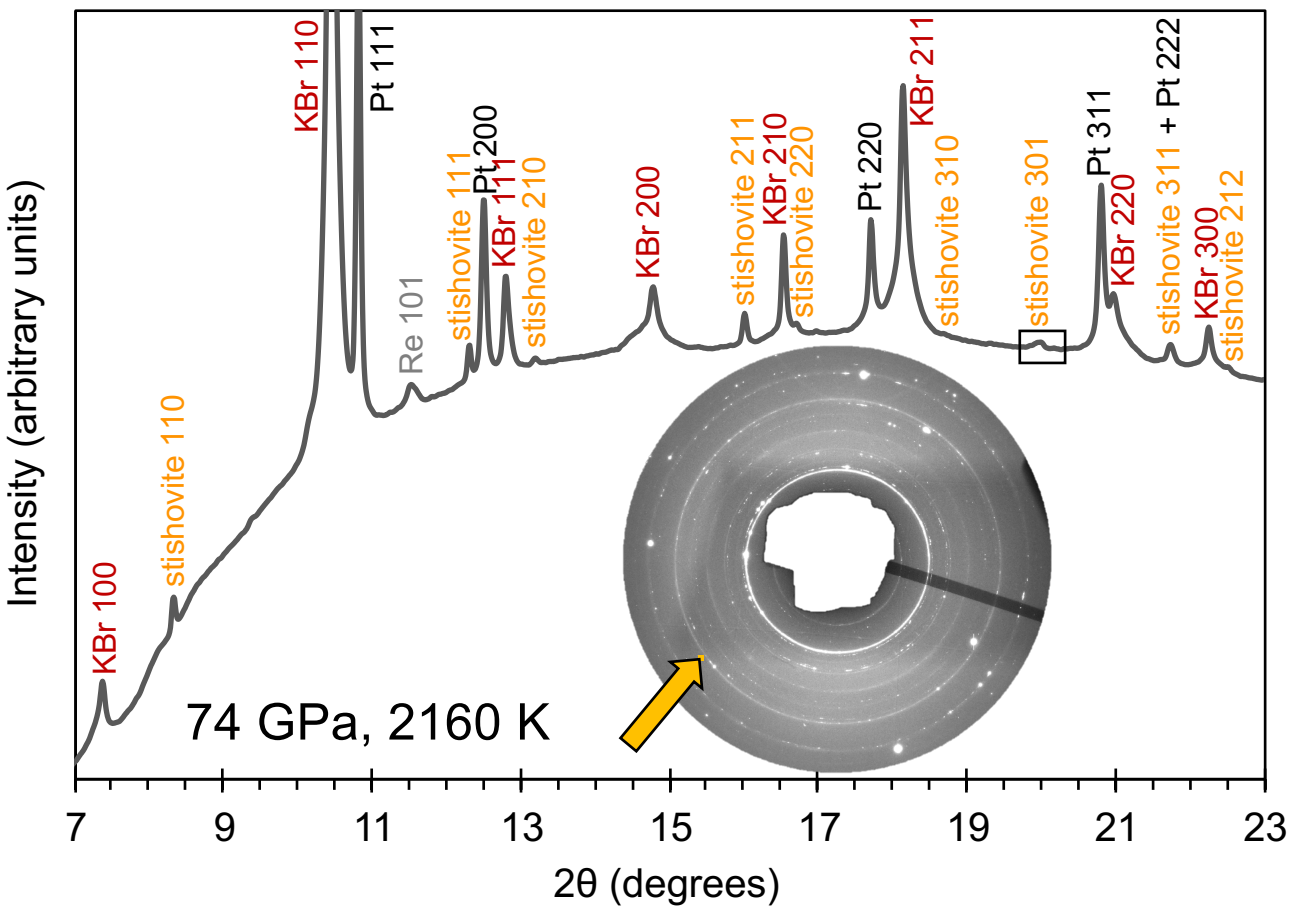
Intensity (arbitrary units)
2θ (degrees)
7
9
11
13
15
17
19
21
23
KBr 100
stishovite 110
KBr 110
Pt 111
Re 101
stishovite 111
Pt 200
KBr 111
stishovite 210
KBr 200
stishovite 211
KBr 210
stishovite 220
Pt 220
KBr 211
stishovite 310
stishovite 301
Pt 311
KBr 220
stishovite 311 + Pt 222
KBr 300
stishovite 212
74 GPa, 2160 K

Figure 2(b)

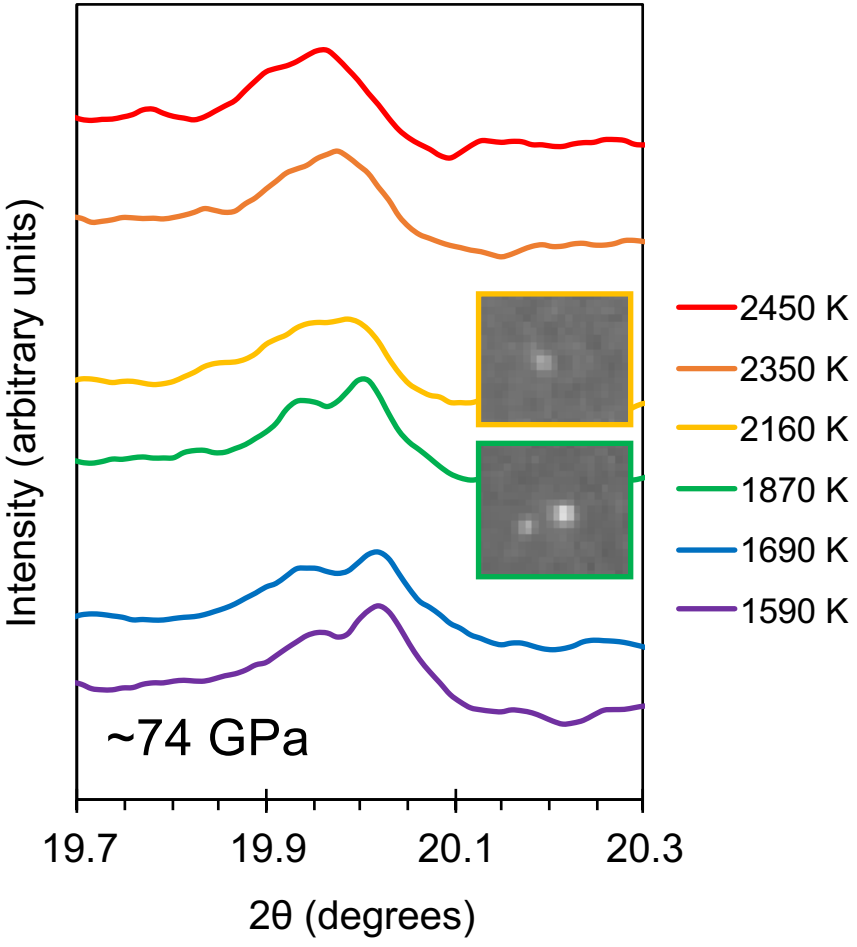
Intensity (arbitrary units)
2450 K
2350 K
2160 K
1870 K
1690 K
1590 K
~74 GPa
19.7
19.9
20.1
20.3
2θ (degrees)

Figure 3

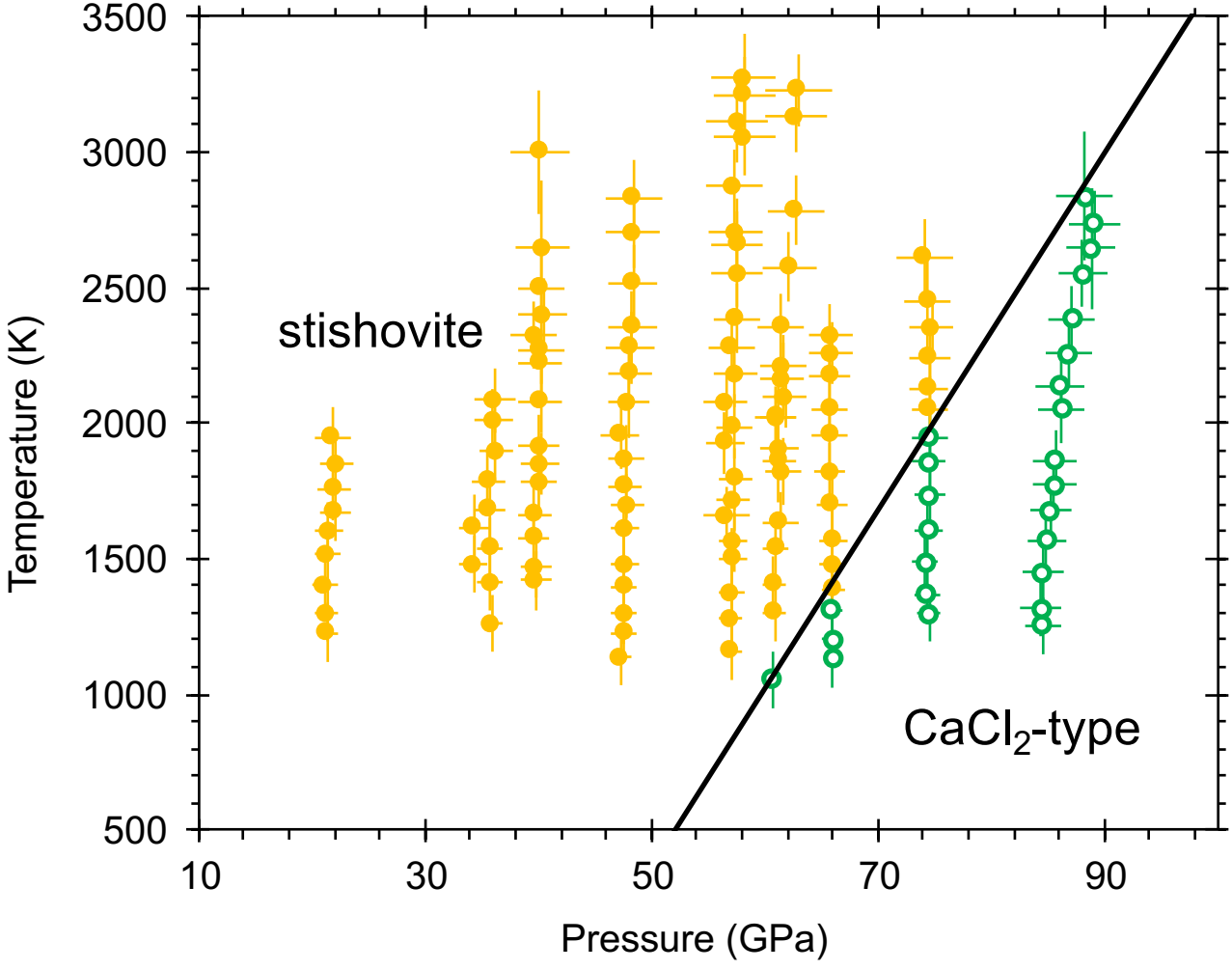
3500
3000
2500
2000
1500
1000
500
Temperature (K)
10
30
50
70
90
Pressure (GPa)
stishovite
CaCl2-type

Figure 4(a)

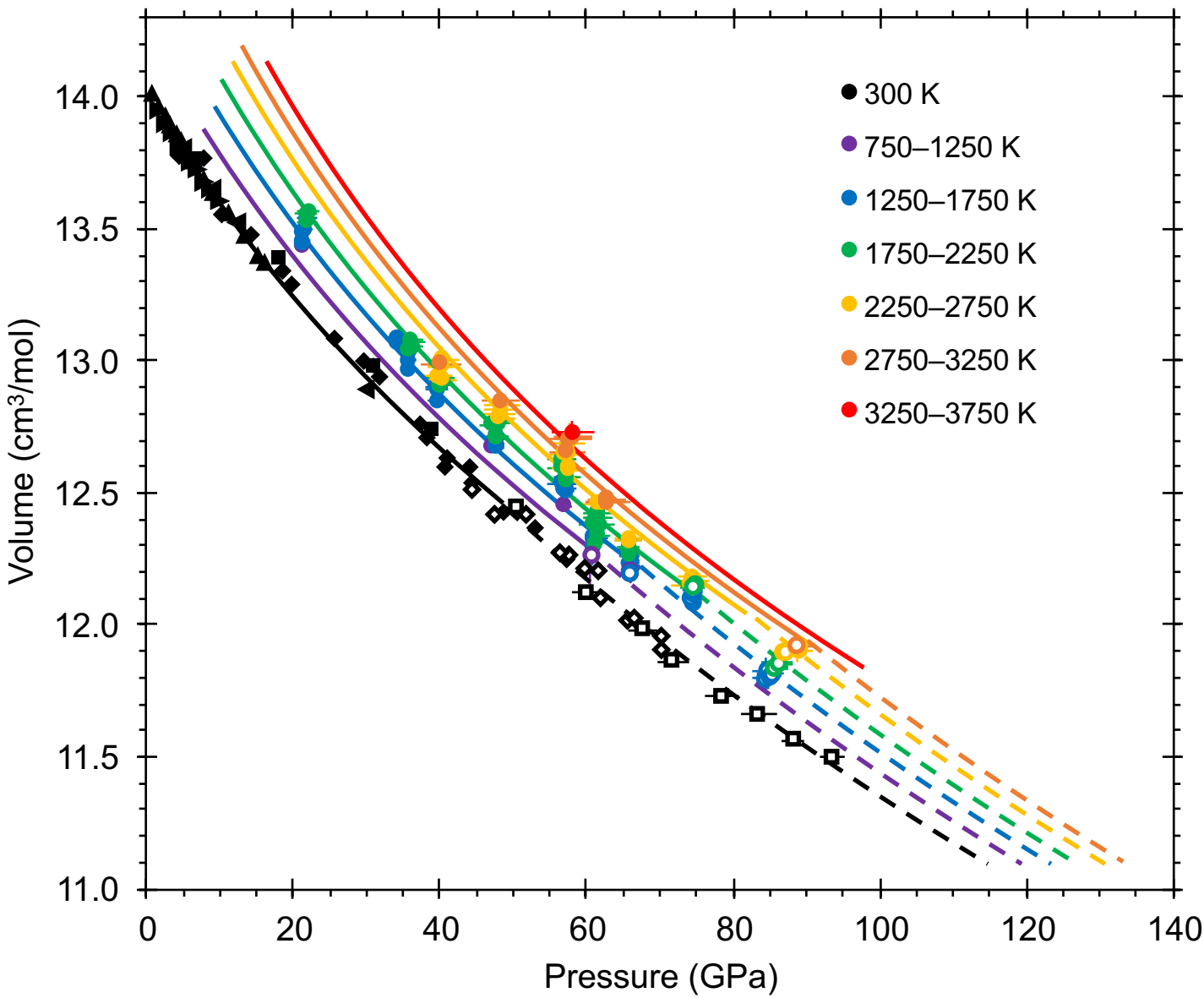
300 K
750–1250 K
1250–1750 K
1750–2250 K
2250–2750 K
2750–3250 K
3250–3750 K
Volume (cm³/mol)
Pressure (GPa)
14.0
13.5
13.0
12.5
12.0
11.5
11.0
0
20
40
60
80
100
120
140

Figure 4(b)

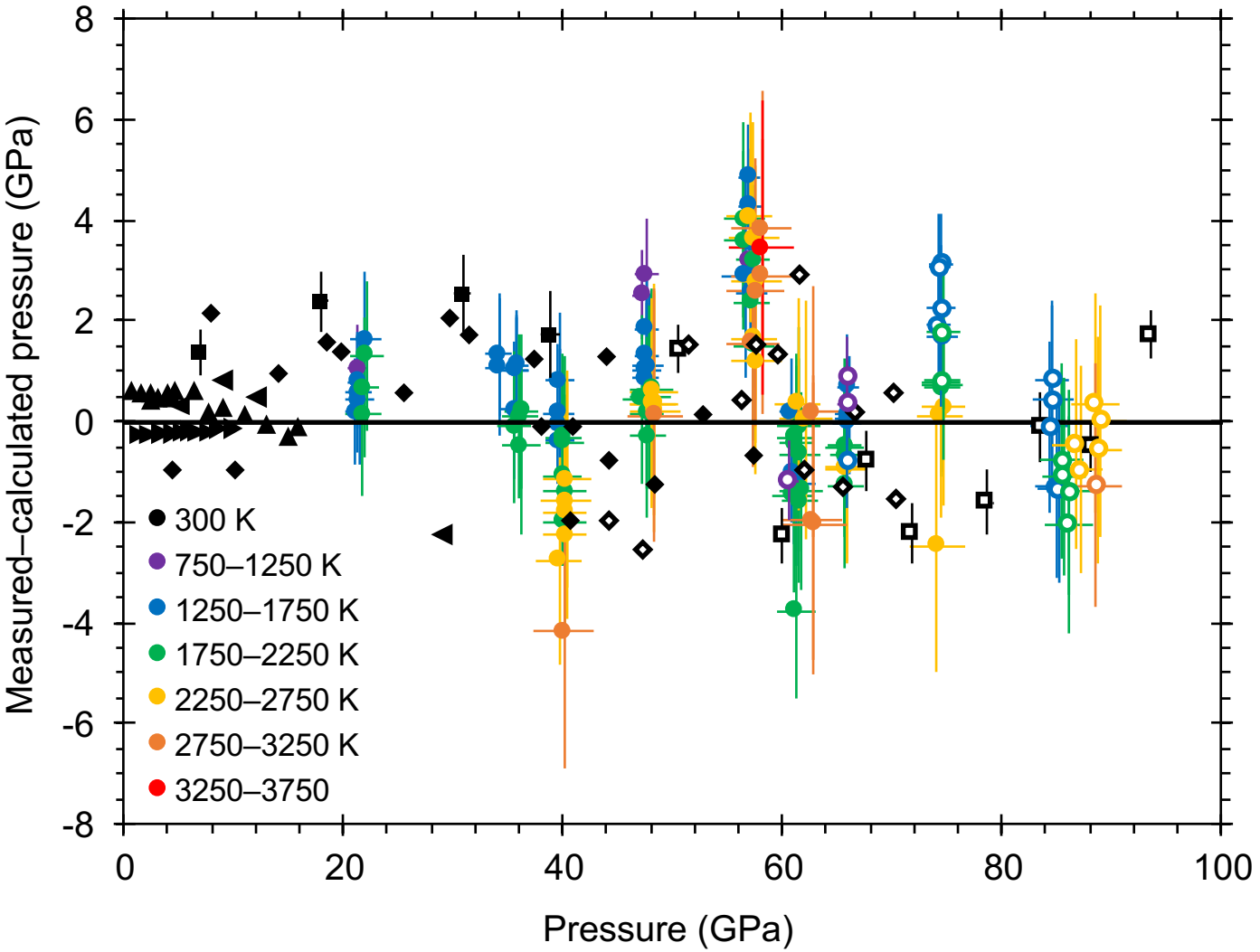
Measured–calculated pressure (GPa)
Pressure (GPa)
8
6
4
2
0
-2
-4
-6
-8
0
20
40
60
80
100
300 K
750–1250 K
1250–1750 K
1750–2250 K
2250–2750 K
2750–3250 K
3250–3750

Figure 5

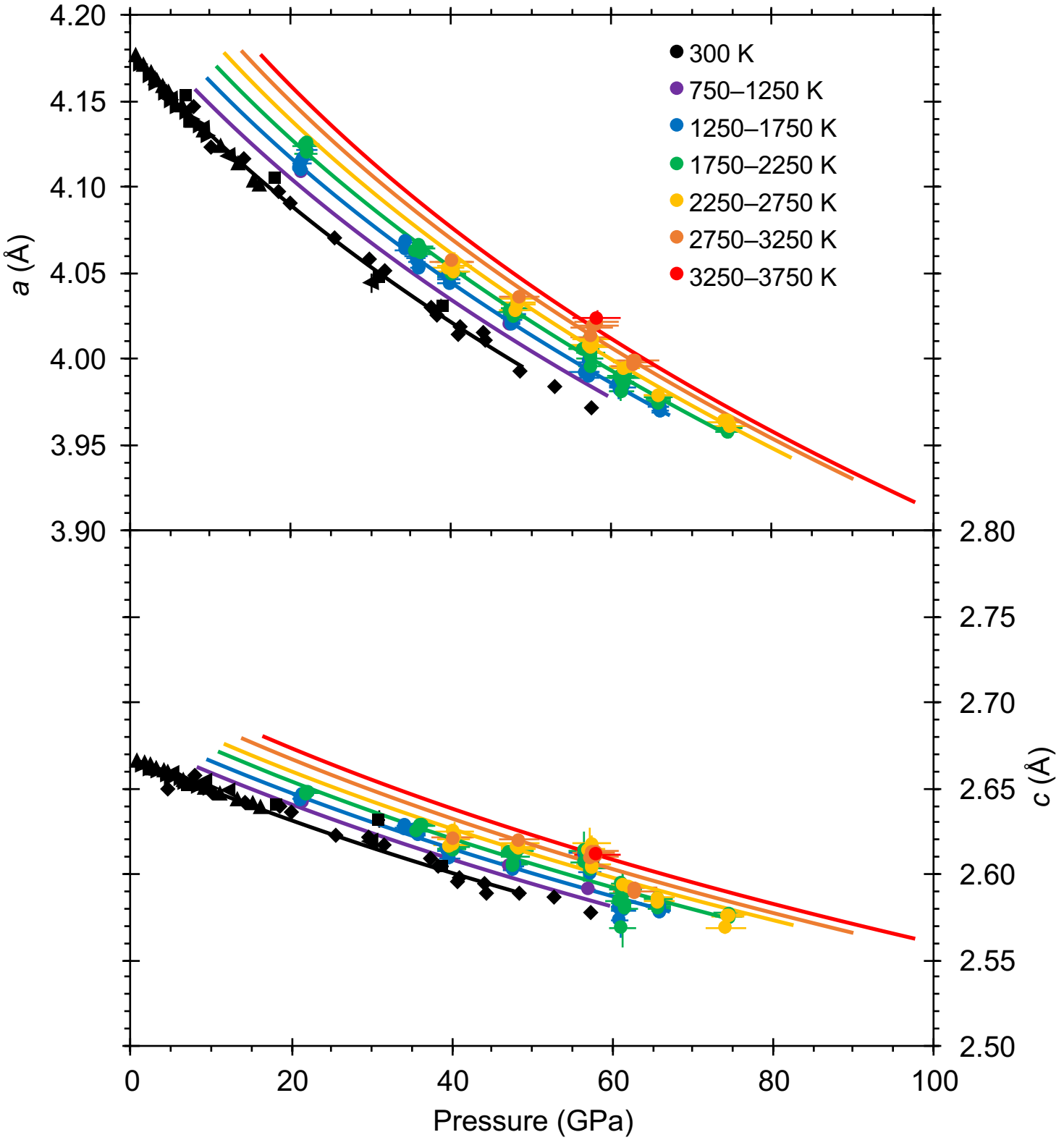
300 K
750–1250 K
1250–1750 K
1750–2250 K
2250–2750 K
2750–3250 K
3250–3750 K
a (Å)
c (Å)
Pressure (GPa)
4.20
4.15
4.10
4.05
4.00
3.95
3.90
2.80
2.75
2.70
2.65
2.60
2.55
2.50
0
20
40
60
80
100

Figure 6

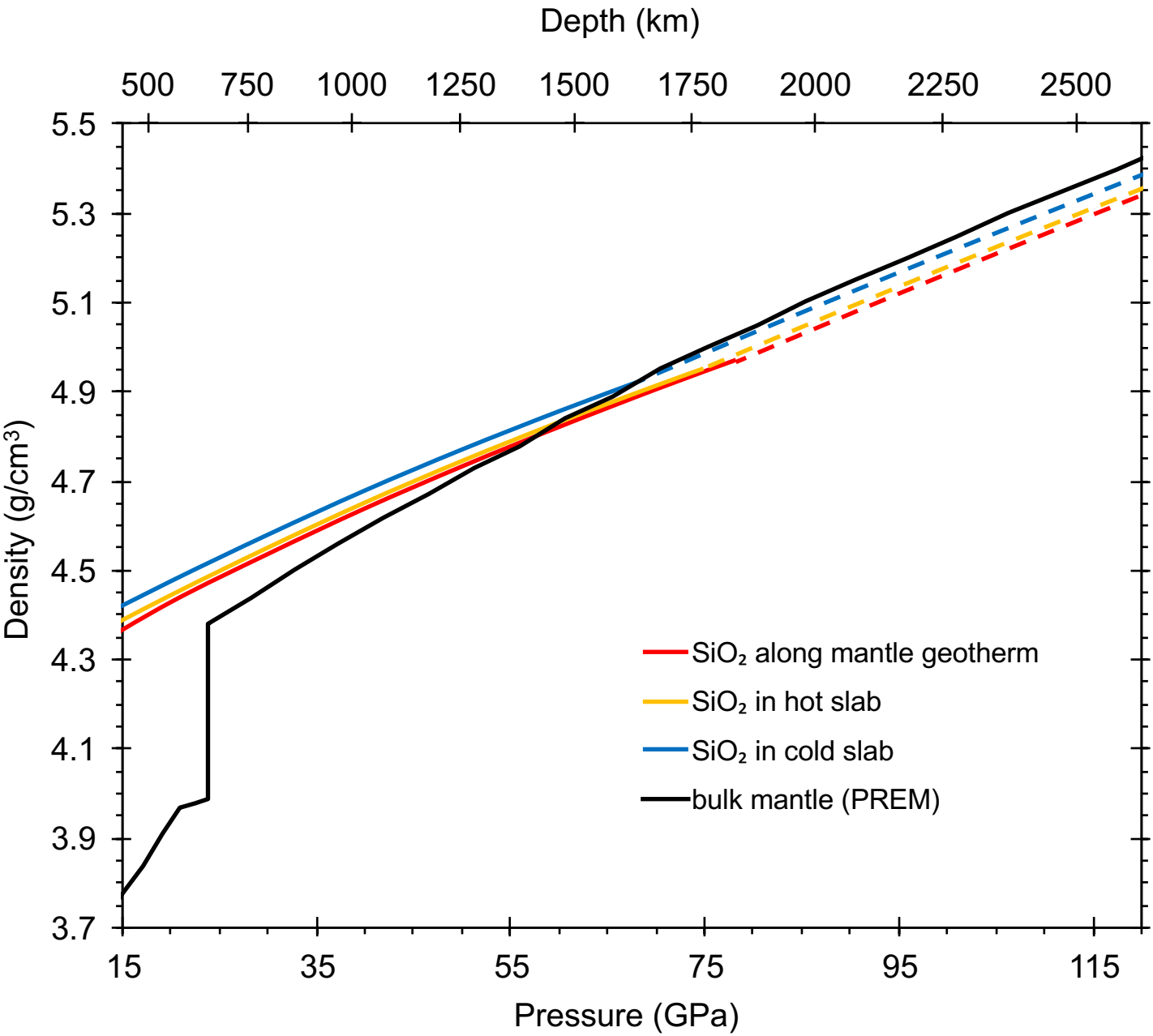
Depth (km)
500
750
1000
1250
1500
1750
2000
2250
2500
5.5
5.3
5.1
4.9
4.7
4.5
4.3
4.1
3.9
3.7
Density (g/cm3)
15
35
55
75
95
115
Pressure (GPa)
SiO2 along mantle geotherm
SiO2 in hot slab
SiO2 in cold slab
bulk mantle (PREM)